

Influence of convective processes on weather research and forecasting model precipitation biases over East Asia

Shiori Sugimoto¹ · Yongkang Xue² · Tomonori Sato³ · Hiroshi G. Takahashi⁴

Received: 26 April 2022 / Accepted: 3 November 2022 © The Author(s) 2022

Abstract

Dynamical downscaling with a 20 km horizontal resolution was undertaken over East Asia for the period May–August in 1991–2015 using the Weather Research and Forecasting (WRF) model with Grell-3D ensemble cumulus parameterization as a product of the Impact of Initialized Land Temperature and Snowpack on Sub-Seasonal to Seasonal Prediction (LS4P) program. Simulated climatological precipitation biases were investigated over land during June when heavy precipitation occurred. Simulations underestimated precipitation along the Meiyu/Baiu rainband, while overestimating it farther north. Dry and wet biases expanded to south and north of the Yangtze River in China, respectively, marking years with poor precipitation simulations. Model biases in synoptic-scale circulation patterns indicate a weakened clockwise circulation over the western North Pacific in the model due to active convection there, and suppressed northward moisture transport to the Meiyu/Baiu rainband. Moisture convergence was slightly enhanced over central China due to an apparent anticyclonic circulation bias over northern China. In years with large biases, positive feedback between reduced moisture inflow and inactive convection occurred over southern China, while moisture transport to central China intensified on regional scales, with amplification of dry and wet biases over China. The Kain–Fritch scheme was used to test the influence of cumulus parameterization, improving the dry bias over southern China due to the modification of synoptic-scale circulation patterns in the lower troposphere. However, precipitation was further overestimated over central China, with the accuracy of precipitation distribution deteriorating.

Keywords East Asia · Precipitation bias · Cumulus parameterization scheme · WRF model

1 Introduction

Most precipitation over East Asia occurs during the Asian summer monsoon season in association with northward movement of a synoptic-scale rainband system known as the Meiyu in China, Baiu in Japan, and Changma in Korea (e.g., Yihui and Chan 2005). Climatologically, precipitation increases over the Yangtze River Basin and southwestern

Shiori Sugimoto shiorisug@jamstec.go.jp

Published online: 21 November 2022

- Japan Agency for Marine-Earth Science and Technology, 3173-25 Showa-machi, Kanazawa-Ku, Yokohama, Kanagawa 236-0001, Japan
- ² University of California, Los Angeles, CA 90095, USA
- Faculty of Environmental Earth Science, Hokkaido University, Sapporo, Japan
- Department of Geography, Tokyo Metropolitan University, Hachioji, Japan

Japan from early to late June, then moves to northern China, Korea, and eastern and northern Japan until mid-July. A synoptic-scale moisture supply along the western fringe of the anticyclonic circulation over the western North Pacific controls precipitation along the Meiyu/Baiu rainband (Ohba et al. 2015; Nguyen-Le et al. 2017; Takahashi and Fujinami 2021).

Annual variations in this synoptic-scale moisture supply are affected by factors such as the global air—sea coupling system (e.g., Sui et al. 2007), snow cover over the Himalayas and Tibetan Plateau (Liu and Yanai 2002; Wu and Qian 2003; Zhao et al. 2007; Seol and Hong 2009; Xiao and Duan 2016), and the eastward propagation of disturbances generated over the Tibetan Plateau (Yasunari and Miwa 2006; Li et al. 2008; Feng et al. 2014; Sugimoto 2020). A new mechanism has been proposed for the regulation of precipitation over downstream of the Yangtze River Basin in which remote impacts of land surface temperature (LST) and subsurface temperature (SUBT) in a geographically upstream region

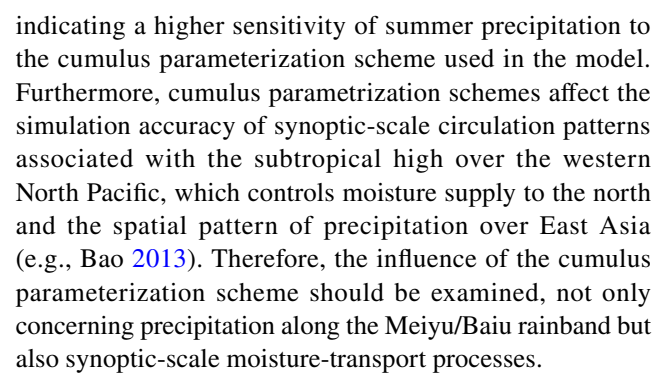


modulate precipitation with an approximately one-month lag (Xue et al. 2018). LST and SUBT over the Tibetan Plateau in May are significantly related to precipitation over the Yangtze River Basin and surrounding regions in June when monthly mean precipitation reaches a maximum due to Meiyu/Baiu rainband activity.

To elucidate the role of such land processes in regulating precipitation in the Yangtze River Basin and its uncertainty for subseasonal-to-seasonal prediction, the Impact of Initialized Land Temperature and Snowpack on Sub-Seasonal to Seasonal Prediction (LS4P) program was launched by the Global Atmospheric System Studies (GASS) panel of the Global Energy and Water Exchanges (GEWEX) project in 2018, with its first phase being undertaken jointly with the Third Pole Experiment (TPE) Earth System Model (ESM) inter-comparison project (TPEMIP). Twenty-one ESM groups participate in the LS4P/TPEMIP program and have already contributed to our understanding of the influence of initializing LST/SUBT over the Tibetan Plateau in ESMs in terms of seasonal to sub-seasonal predictions of precipitation over East Asia (Xue et al. 2021). In addition, several Regional Climate Model (RCM) groups participating in the LS4P/TPEMIP program provide fundamental understanding of water and energy cycles across East Asia.

The RCMs are powerful tools in the study of regionalscale atmospheric conditions and physical processes and their effects on regional climate, with the potential to clarify scientific issues featured in the LS4P/TPEMIP program. High-resolution experiments with convectionpermitting configurations have been widely undertaken, but experiments concerning long-term climatological studies and large domain settings are feasible only with resolutions of tens of kilometers, as in the products of the Coordinated Regional Climate Downscaling Experiment (CORDEX; e.g. Yu et al. 2020 for the East Asian region; for other references, see https://cordex.org/publications/) and the database for Policy Decision making for Future climate change (d4PDF; Mizuta et al. 2017; Fujita et al. 2020). Such climatological products need careful evaluation because biases may be included in the spatial resolution and physical schemes. In particular, simulations with horizontal mesh sizes greater than several kilometers require cumulus parameterization schemes to evaluate the effects of sub-grid-scale convective processes.

Previous studies comparing East Asian precipitation simulations based on models using different cumulus parameterization schemes have revealed differences in the amount, frequency, intensity, and diurnal variation of precipitation (Shing et al. 2006; Choi et al. 2015; Zhang et al. 2015; Huang and Gao 2017; Cai et al. 2018; Niu et al. 2020). The proportion of convective precipitation relative to total precipitation over East Asia may be higher during summer than in other seasons (Zhang et al. 2015),



In this study, numerical experiments were undertaken for the East Asia region during the May-August period for 25 years (1991-2015) as a product of LS4P/TPEMIP program, and the simulated monthly precipitation evaluated against reference observational datasets. Analyses were undertaken mainly over land because reliable high-resolution observational datasets are available only over land in East Asia. We focused particularly on precipitation biases during June because more precipitation is observed during this month over the Yangtze River Basin and surrounding regions in association with the Meiyu/Baiu rainband, sometimes causing serious flooding as 1998 and 2020. Atmospheric factors causing biases in climatological precipitation were identified, and atmospheric circulation patterns in years with large precipitation biases were also investigated to elucidate the reasons that amplify the climatological biases. An experiment using another cumulus parameterization scheme was undertaken to investigate the possible influence of convection process on June precipitation biases over land.

2 Numerical setup and data

Numerical experiments with 20 km horizontal resolution were undertaken for 1991-2015 using the Weather Research and Forecasting (WRF) model v. 3.9.1.1 (Skamarock et al. 2008) as a product for the LS4P/TPEMIP program. The experiments were integrated from 00:00 UTC April 21 to 00:00 UTC September 1 for each year, with the simulation domain covering most of South and East Asia (Fig. 1). The analysis period was from 00:00 UTC May 1 to 23:00 August 31, with the precipitation in June being intensively investigated over East Asia (20°-47°N, 100°-150°E). The model has 50 vertical layers of non-uniform thickness with an upper boundary of 50 hPa. The time step was 10 s, and the output interval 1 h. Physical schemes used in the experiment were the Dudhia scheme for shortwave radiation (Dudhia 1989), the rapid radiative transfer model for longwave radiation (Mlawer et al. 1997), the Mellor-Yamada Nakanishi-Niino 2.5 level turbulence kinetic energy scheme for planetary boundary layer condition (Nakanishi and Niino 2004, 2006), the unified Noah land-surface scheme (Chen



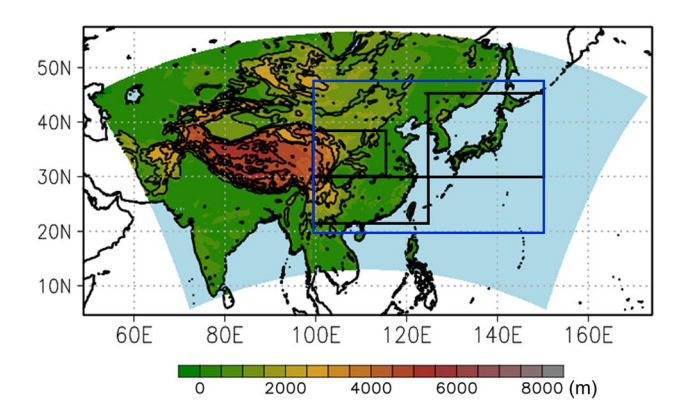


Fig. 1 Topography in the calculation domain (shaded and contour). The contour interval is 1000 m. Light blue indicates water. Blue rectangle indicates the analysis area (East Asia; $20^{\circ}-47^{\circ}N$, $100^{\circ}-150^{\circ}E$); black rectangles indicate subregions; southern-southeastern China ($21^{\circ}-30^{\circ}N$, $100^{\circ}-125^{\circ}E$), central China ($30^{\circ}-39^{\circ}N$, $100^{\circ}-115^{\circ}E$), and Japan and Korea ($30^{\circ}-45^{\circ}N$, $125^{\circ}-150^{\circ}E$). The Yangtze River lies along $\sim 30^{\circ}N$ in China

and Dudhia 2001), the Thompson scheme for microphysics (Thompson et al. 2008), and the Grell-3D ensemble scheme (Grell 1993; Grell and Devenyi 2002) for cumulus parameterization. We also undertook experiments using the Kain–Fritch (KF) scheme (Kain 2004) rather than the Grell-3D ensemble scheme, results of which are discussed in Sect. 4. Herein, the original experiment is referred to as the Grell-3D experiment, and another experiment as the KF experiment.

Here, we briefly introduce the Grell-3D ensemble and KF schemes. The Grell-3D ensemble scheme basically adopts three dynamic control assumptions, which are two types of closures assuming environmental stability, i.e., quasi-stability equilibrium and instantaneous stability, and a type of closure relates to total moisture convergence. Each dynamic control assumption has several subensembles considering perturbation of key parameters. For all these sub-ensembles, processes to modify atmospheric environment by convection are estimated, in which fractional entrainment/detrainment rates and downdraft mass flux are perturbed. Then, an ensemble mean of results from subensembles are calculated appropriately. Meanwhile, the KF scheme considers only instantaneous stability, which identifies layers with potential source for convection at first as the trigger function to compare temperature between the parcel at the lifting condensation level (LCL) and its ambient. If the parcel is sufficiently warmer than its ambient environment, it candidates for deep convection. Vertical velocity of the parcel above the LCL is estimated by the Lagrangian parcel method considering entrainment, detrainment, and water loading. Mass in a column is adjusted until at least 90% of convective available potential energy

(CAPE) is removed. Please refer to Grell (1993), Grell and Devenyi (2002), Kain (2004) and related papers for the detail of these schemes.

The ERA interim reanalysis of the European Centre for Medium-Range Weather Forecasts (ECMWF) with $1.5^{\circ} \times 1.5^{\circ}$ resolution (Dee et al. 2011) was used as initial conditions and lateral atmospheric boundaries at 6 h intervals. Sea surface temperatures obtained from the daily Optimum Interpolation Sea Surface Temperature v2 (OISST v2; $0.25^{\circ} \times 0.25^{\circ}$ resolution; Reynolds et al. 2007) were used as lower boundary condition. The OISST v2 using only Advanced Very-High-Resolution Radiometer (AVHRR) was selected to retain uniform data quality throughout the study period.

Precipitation biases between observation and model experiment were examined mainly over land using the dataset of gridded rain-gauge observations of 0.25° × 0.25° resolution produced by the Asian Precipitation-Highly Resolved Observational Data Integration Towards Evaluation of Water Resources/the Asian Precipitation-Highly Resolved Observational Data Integration Towards Evaluation of Extreme Events projects (APHRODITE/APHRDITE-2 V1101R1; Yatagai et al. 2009, 2012). The Climate Prediction Center (CPC) Merged Analysis of Precipitation with $2.5^{\circ} \times 2.5^{\circ}$ resolution (CMAP; Xie and Arkin 1997) was used supplementally to elucidate precipitation biases over the ocean. The National Oceanic and Atmospheric Administration (NOAA) interpolated Outgoing Longwave Radiation (OLR) of 2.5° × 2.5° resolution (Liebmann and Smith, 1996) and the ERA-interim dataset were used for analysis of atmospheric conditions attributable to simulated precipitation biases in June over land. Model output was re-gridded to the resolution of observational or reanalysis datasets for calculation of pattern correlation coefficients, root mean square error (RMSE), and standard deviations of spatial patterns.

3 Results

3.1 Biases in climatological monthly precipitation in the Grell-3D experiments

Spatial distributions of monthly mean climatological precipitation for 1991–2015 were compared between the APHRODITE dataset and Grell-3D experiments for May–August (Fig. 2). An evaluation using the CMAP dataset is also shown in Fig. S1 to complement information for precipitation biases over the ocean. Although we focused on June precipitation over land, precipitation biases in other months are introduced briefly here to elucidate the overall



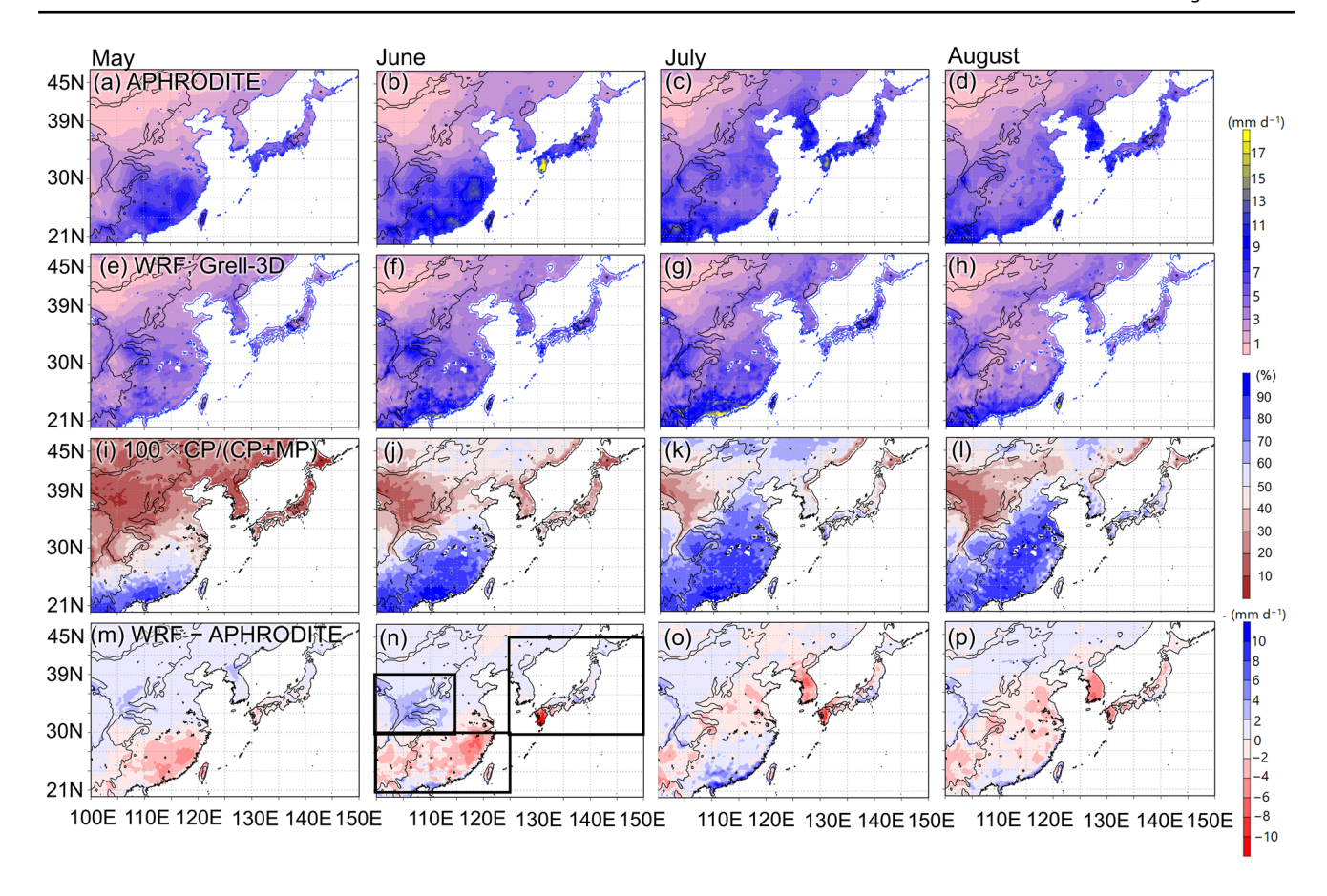


Fig. 2 Spatial distribution of monthly mean precipitation during ${\bf a}$ May, ${\bf b}$ June, ${\bf c}$ July, and ${\bf d}$ August in APHRODITE. ${\bf e}{-}{\bf h}$ As for $({\bf a}{-}{\bf d})$, but for the Grell-3D experiment. ${\bf i}{-}{\bf l}$ As for $({\bf a}{-}{\bf d})$, but for the ratio of precipitation from cumulus parametrization to the total

precipitation. **m**–**p** As for (**a**–**d**), but for precipitation biases (WRF—APHRODITE). Black lines are the 1000 and 3000 m topographic contours. Ocean is masked with white. Black rectangles in (**n**) indicate the subregions, as shown in Fig. 1

simulation skill for precipitation over East Asia in the Grell-3D experiment.

In the APHRODITE dataset, heavier precipitation was observed over southern-southeastern China in May in association with formation of the Meiyu/Baiu rainband (Fig. 2a; an extension of the rainband is shown in Fig. S1). Precipitation observed along the rainband intensified in June and moved northward in July (Fig. 2b, c), which is a typical seasonal movement of the rainband in East Asia. Although the structure of the rainband disappeared in August, heavier precipitation remained over Korea, southwestern Japan, and coastal regions of China (Fig. 2d). Seasonal variation in CMAP precipitation is consistent with that in APHRODITE precipitation (Fig. S1a–d).

Simulated precipitation increased over central China and part of southern China in May (Fig. 2e), intensifying during June particularly northern edge of the Sichuan Basin and southern coastal region in China as well as southwestern Japan (Fig. 2f). This seasonal intensification is consistent with that in APHRODITE, although the Grell-3D experiment underestimated precipitation along the Meiyu/

Baiu rainband in May and June, and overestimating it, particularly over central China, in June (Fig. 2m, n). As a result, dry and wet biases appeared respectively south and north of 30°N over China during June. A possible reason causing the underestimation of the Meiyu/Baiu precipitation would be a weakening of simulated anticyclonic circulation over the western North Pacific, of which detail will be discussed in Sect. 3.3. In July, the northward shift of the Meiyu/Baiu rainband was not simulated well (Fig. 2g), with the area with underestimated precipitation shifting to central China, Korea, and part of Japan (Fig. 20). After retreat of the rainband in August, the simulated precipitation tended to decrease over southern-central China, Korea, and Japan relative to that in the previous month (Fig. 2h), with dry biases appearing (Fig. 2p). Comparison with CMAP provided an additional information over the ocean, i.e., overestimated simulated precipitation south of the rainband, with both wet and dry biases being larger over the western North Pacific than in other regions (Fig. S1e–h, m–p).

The pattern correlation coefficient and RMSE were calculated for monthly precipitation between APHRODITE



and the Grell-3D experiment. Higher correlation coefficients and lower RMSEs were found in May (0.71 and 1.50 mm d^{-1}) and June (0.68 and 2.41 mm d^{-1}) than July (0.46 and 3.43 mm d^{-1}) and August (0.48 and 2.57 mm d^{-1} ; Table 1), indicating the higher simulation skill for the spatial distribution of precipitation in the former months. When CMAP was used instead of APHRODITE, pattern correlations are poorer in May, June, and July, with higher RMSEs in May and June (Table 1), consistent with the larger biases over the ocean (Fig. S1m-o). Although both correlation coefficient and RMSE gradually deteriorated from May to July as an increase in leading time of simulation, they are slightly improved in August. Higher precipitation area shifts to north in sub-monthly scale in July associated with the Meiyu/Baiu rainband propagation (Figs. 2c and S1c), which was quite difficult to simulate in the Grell-3D experiment (Figs. 2g and S1g). Meanwhile, convective precipitation is dominant under the condition with strong surface heating in August climatologically, for which the simulation is easier than the Meiyu/Baiu precipitation in the model experiment using a cumulus parameterization scheme. Therefore, correlation coefficient and RMSE for spatial pattern of July precipitation was worse in comparison to that in August.

In the Grell-3D experiment, total precipitation was calculated from the sum of precipitation from the cumulus parameterization and microphysics schemes. The precipitation from each scheme was quantified using the proportion of precipitation from the cumulus parameterization scheme relative to the total precipitation (Fig. 2i–l over land, and Fig. S1i–l over both land and ocean). In May, > 60% of precipitation was formed in the cumulus parameterization scheme south of 27°N (Fig. 2i). As the month proceeded, the area dominating precipitation from the cumulus parameterization scheme expanded northward, reaching about 36°N in August (Fig. 2j–l).

Table 1 The correlation coefficient (Corr) and the RMSE for the spatial distribution of the climatological precipitation over East Asia for each month between the model experiments and the observations

		May	June	July	August
Grell-3D					
APHRODITE	Corr	0.71	0.68	0.46	0.48
	RMSE	1.50	2.41	3.43	2.57
CMAP	Corr	0.51	0.48	0.36	0.68
	RMSE	2.23	2.88	2.96	2.46
KF					
APHRODITE	Corr	0.74	0.72	0.48	0.65
	RMSE	2.28	2.98	3.95	3.46
CMAP	Corr	0.56	0.63	0.50	0.61
	RMSE	2.14	2.85	3.49	2.62

This indicates that underestimation of precipitation along the Meiyu/Baiu rainband was caused by the cumulus parameterization scheme, while microphysics precipitation was more dominant over land with a wet bias.

To summarize, for precipitation biases in the Grell-3D experiment with a 20 km spatial resolution over East Asia, the major factor is the combination of the dry bias along the Meiyu/Baiu rainband and the wet bias north and south of it, as recognized not only in June but also in May and July. Focusing on June precipitation over land, these dry and wet biases are clearly identified over China, particularly south and north of the Yangtze River (30°N). The underestimation of precipitation over southern-southeastern China was influenced by the cumulus parameterization scheme, while its overestimation over central China was associated with the microphysics scheme. Annual variations in June precipitation biases and the relationships between atmospheric circulation patterns and June precipitation biases are considered in the following sections.

3.2 Yearly biases in June precipitation over land

Area-averaged precipitation over land during June in East Asia (20°–47°N, 100°–150°E) was compared between APHRODITE and Grell-3D experiment. The 25-yr mean was 4.29 mm d⁻¹ in APHRODITE and 4.13 mm d⁻¹ in the Grell-3D experiment (Table S1), with area-averaged climatological precipitation thus being comparable between observations and the model, although with spatially distributed dry–wet biases as explained in Sect. 3.1. Yearly variations in area-averaged precipitation were also simulated reasonably well in the Grell-3D experiment (Fig. 3a), with standard deviations in interannual variations of 0.41 mm d⁻¹ for observations and 0.64 mm d⁻¹ for the model and a temporal correlation coefficient of 0.57 (Table S2).

East Asia was divided into three subregions based on the spatial distribution of climatological precipitation biases (Fig. 2n): southern-southeastern China (21°-30°N, 100°-125°E), central China (30°-39°N, 100°-115°E), and Japan and Korea (30°-45°N and 125°-150°E; rectangles in Figs. 1 and 2n). Yearly variations in precipitation averaged over land in these subregions are shown in Fig. 3b-d. Simulated precipitation over southern-southeastern China was lower than observed in 16 of the 25 years (Fig. 3b), and higher over central China for 24 years (Fig. 3c). This indicates that the dry and wet biases south and north of the Yangtze River, as shown in climatological mean precipitation (Fig. 2n), were not attributable to specific years but were uniform across all years. Analysis of pentad precipitation (Fig. 4a) indicates that the dry bias over southern-southeastern China was more obvious during early June, while the wet bias over central China occurred consistently between first and fourth pentads although each



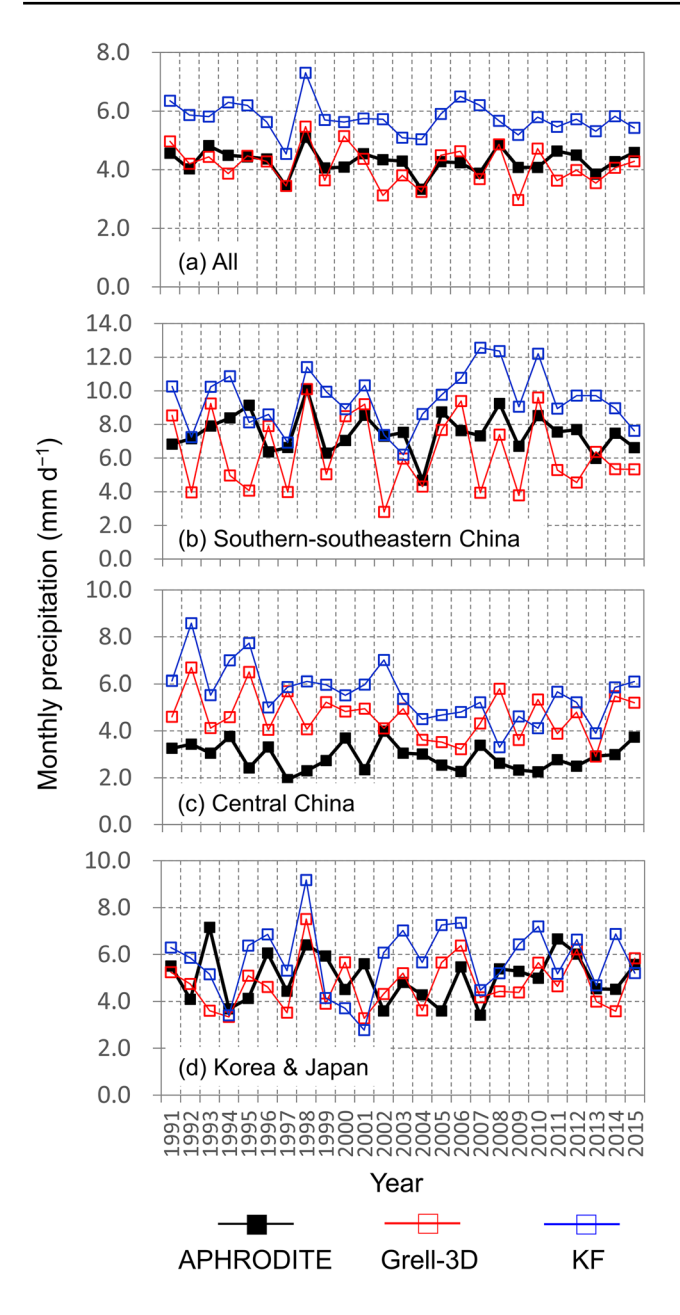


Fig. 3 Yearly variations in precipitation from APHRODITE (black) and WRF model experiments (Grell-3D, red; KF, blue) averaged over land in **a** East Asia, **b** southern-southeastern China, **c** central China, and **d** Korea and Japan. Subregions in **b**–**d** are as in Fig. 1

pentad included 3–5 years of dry bias. The increase in wet bias over central China tended to follow the appearance of dry biases over southern-southeastern China. Over Japan and Korea, the precipitation bias varied by year, with the area-averaged precipitation bias being smaller than those of the other two subregions (Fig. 3d). The temporal correlation coefficient in area-averaged precipitation between APHRODITE and the Grell-3D experiments is 0.41 over southern-southeastern China, -0.01 over central

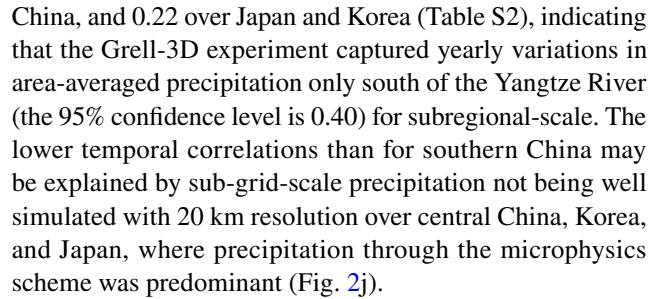


Figure 5 shows interannual variations in pattern correlation coefficients and RMSEs for June precipitation over land in East Asia. RSMEs were within 2.5–5.0 mm d⁻¹ for all 25 years, with correlation coefficients of 0.13–0.70. There are seven years (1992, 1995, 1997, 1999, 2002, 2004, and 2007) for which the correlation is insignificant (i.e., coefficient < 0.4), defined here Lower Correlation Coefficient (LowCC) years. As shown in a Taylor diagram, the LowCC years correspond to years of poor simulation skill (Fig. S2).

Characteristics of the spatial distribution of June precipitation biases over land in LowCC years were confirmed visually (Fig. S3). In 1992, 1995, 1997, 2002, and 2007, the simulated June precipitation was underestimated south of 30°N in China and overestimated in regions farther north. In fact, the positive precipitation bias north of the Yangtze River was also existed in other LowCC years (i.e., 1999 and 2004). Meanwhile, the dry bias was concentrated over the Yangtze River (i.e., along ~ 30°N) as well as the southern part of Korea and southwestern Japan. These results suggest that dry and wet biases in regions south and north of the Yangtze River, respectively, were more intensified in LowCC years than apparent climatologically. Over Korea, Japan, and north of 39°N, a common characteristic of precipitation bias was not found in LowCC years.

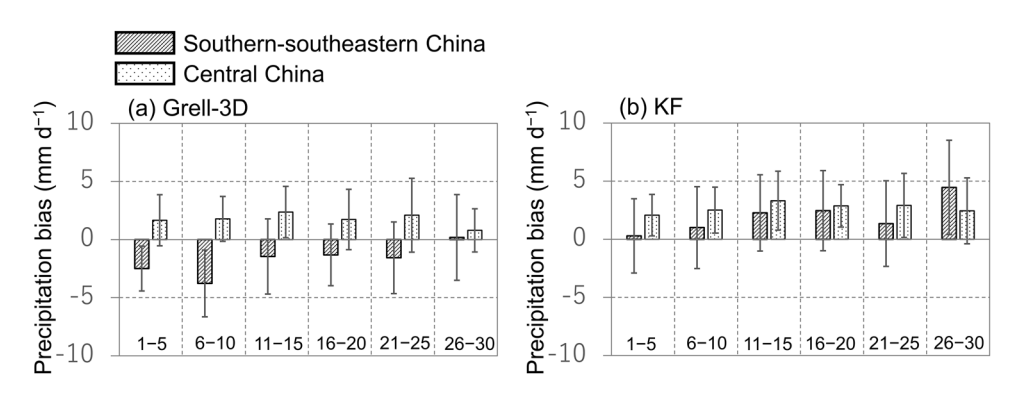
3.3 Climatological biases in atmospheric circulation patterns

Detailed analysis of June precipitation biases over land in East Asia revealed two characteristics: systematic dry and wet biases south and north of the Yangtze River, respectively; and their intensification in particular years when the precipitation distribution was poorly simulated (i.e., LowCC years). Therefore, we examined climatological biases in the atmospheric circulation pattern during June to elucidate the systematic dry/wet biases over East Asia in this section. Atmospheric features in LowCC years are analyzed in the next section.

Figure 6a shows the June climatology of geopotential height and moisture fluxes at 850 hPa from the ERA-interim and OLR from the NOAA interpolated OLR datasets. The subtropical high expanded over the western North Pacific and transported moisture to East Asia. Monsoon westerlies passing over South and Southeast Asia also supplied



Fig. 4 The bias in climatological five-day precipitation in June (bars indicate WRF model experiments minus APHRODITE) averaged over land in southern-southeastern China and central China. a Grell-3D experiment; b KF experiment. Error bars indicate one standard deviation for the 25-year period



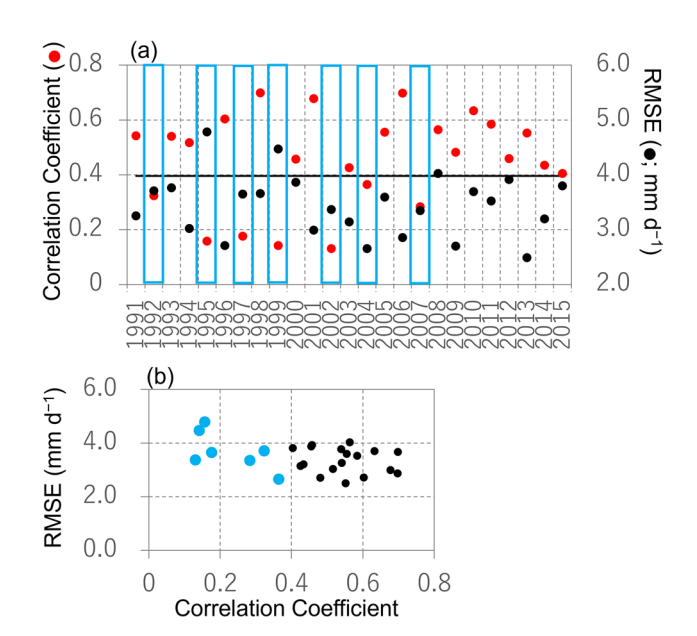


Fig. 5 a Yearly variations in correlation coefficient and RMSE for the spatial distribution of June precipitation over land in East Asia for the Grell-3D experiment; **b** scatter-diagram for each year. Black line in (**a**) indicates the 95% confidence level for the correlation coefficient

moisture from tropical regions to East Asia. Convection was active along the Meiyu/Baiu rainband and over South and Southeast Asia.

In the Grell-3D experiments, the subtropical high over the western North Pacific was weaker than in the ERA-interim data, corresponding to more active convection in the model (Fig. 6b). Large-scale circulation patterns include low-high-low biases in geopotential height at 850 hPa from the western North Pacific to northern Japan, which seem to be a northward propagation of quasi-stationary waves similar to the Pacific–Japan (PJ) teleconnection pattern (e.g. Nitta 1987). The weaker clockwise circulation over the western North Pacific in the model suppressed moisture inflow toward the Meiyu/Baiu rainband as well as southern-southeastern China, suggesting that this is a factor to cause

the underestimation of June precipitation along the rainband as described in Sect. 3.1.

Meanwhile, moisture convergence was slightly enhanced at 850 hPa over central China (30°-35°N, 105°-120°E) due to anticyclonic circulation biases over northern China, which is consistent with active convection there relative to that in observations (Fig. 6b). In the upper troposphere, the Grell-3D experiment can simulate climatological features of wind field at 200 hPa (Fig. S4); however, the jet stream meandering between 30°N-40°N was emphasized in the model relative to that in the reanalysis dataset, and westerly wind was intensified along ~27.5°N where wind speed was weak in the reanalysis. As a result, lower geopotential height biases expanded widely at 200 hPa west of 100°E, likely induced by quasi-stationary wave propagation along the subtropical jet (Fig. 6c, d). This result corresponds to Ding and Wang (2005, 2007), which indicated that the active convection over the Indian subcontinent enhances upperlevel positive height anomaly over the Tibetan Plateau and induces wave train propagating along the subtropical jet. Geopotential height biases at 200 hPa around the Tibetan Plateau are possibly associated with inactive convection over South Asia, which also affects geopotential height biases over northern China at 850 hPa leading to the enhanced moisture convergence over central China.

Thus, biases in synoptic-scale circulation patterns expanding across the whole domain seem to be associated with convective activity particularly over the western North Pacific and South Asia. Synoptic-scale circulation patterns in the upper troposphere also may be important in simulating the location of the Meiyu/Baiu rainband as well as moisture transport from the south in the lower troposphere as discussed in Sato and Xue (2013).

3.4 Anomalies in atmospheric circulation patterns in LowCC years

Differences in atmospheric circulation patterns between LowCC years and the climatology were investigated over East Asia to determine why dry/wet biases south and north of the Yangtze River are more pronounced in LowCC



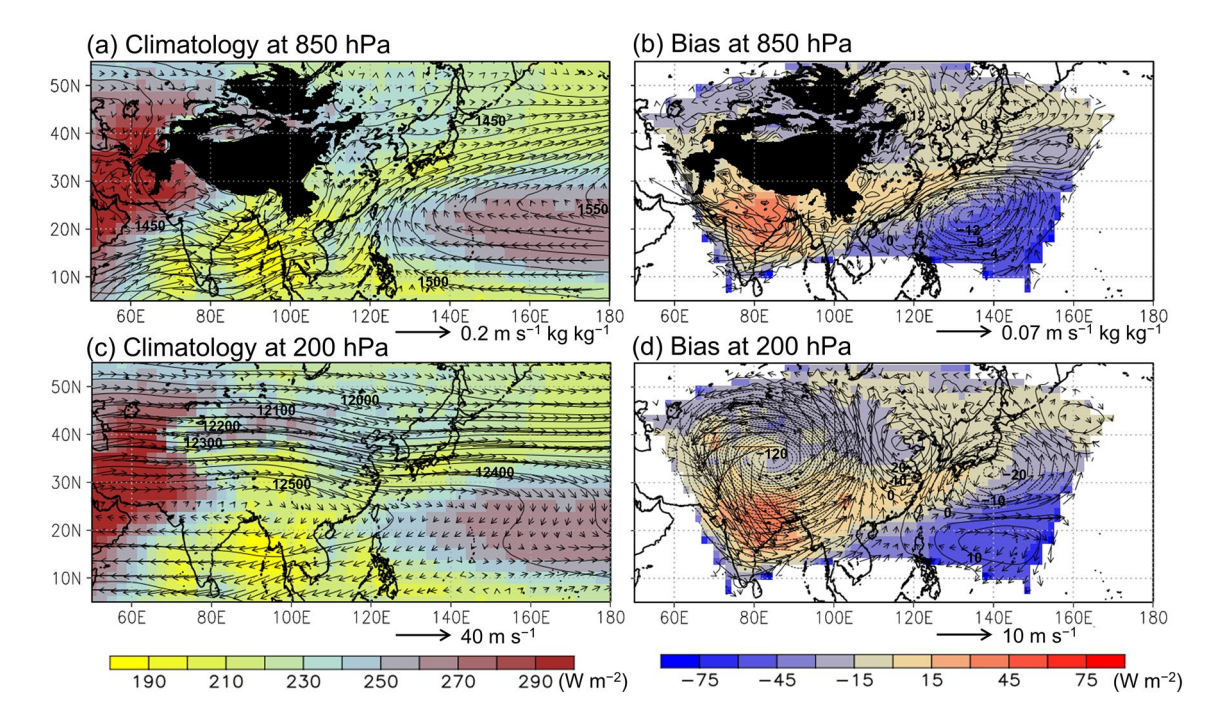


Fig. 6 a Spatial distribution of the ERA-interim climatology for moisture flux (vectors) and geopotential height (contours) at 850 hPa in June 1991–2015. Shading indicates the OLR in NOAA interpolated OLR datasets. **b** Spatial distribution of biases in the climatological moisture flux (vectors) and geopotential height

(contours) at 850 hPa, and OLR (Grell-3D experiment minus ERA-interim or NOAA interpolated OLR). **c**, **d** As for (**a**, **b**) but for 200 hPa and wind rather than moisture flux. Shading in (**c**, **d**) is as for (**a**, **b**). Topography above 1200 m is masked in (**a**, **b**). Lateral boundary conditions may affect results near the boundary

years. In the ERA-interim dataset, LowCC years show positive anomalies in geopotential height over northern China at 850 hPa (Fig. 7a), as also captured at 500 and 200 hPa (although not statistically significant; Fig. 7b, c). Negative anomalies in geopotential height were located over the western North Pacific at 850, 500, and 200 hPa. These positive and negative anomalies in geopotential height during LowCC years correspond respectively to inactive and active convection at each location relative to that in the climatology (not shown). As these anomalies have the same sign as climatological biases in geopotential height shown in Fig. 6b, d, we speculate that climatological biases of geopotential height were intensified in LowCC years causing further weakening of moisture transport at 850 and 500 hPa over the coastal region of southeastern China and off its coast (Fig. 7a, b).

A higher geopotential height anomaly over northern China and a lower anomaly over the western North Pacific were also captured at each vertical level during LowCC years in the Grell-3D experiments, suppressing moisture supply to southern China (although the anomalies are not statistically significant except for northern China at 850 hPa; Fig. 7d–f). Geopotential height and moisture flux anomalies in the model experiments were basically driven by the ERA-interim dataset as external forcing. In addition to these anomalies, the WRF model yielded significantly

intensified positive geopotential height anomaly over southern-eastern China at 850 hPa and negative anomaly over southern China at 200 hPa relative to those in the ERA-interim. These anomalies over southern-eastern China can be explained by the weakening of moisture transport over southeastern China and off its coast, forced by ERAinterim, which suppresses convection and precipitation over southern-southeastern China. As a result, positive and negative geopotential height anomalies were intensified in the lower and upper troposphere, respectively. Positive feedback would also have occurred among the reduction in moisture inflow, inactive convection, and intensification of the positive geopotential height anomaly at 850 hPa. In association with the development of the anticyclonic circulation anomaly over southeastern China at 850 hPa, northward moisture transport was activated over the eastern Sichuan Basin (28°–33°N, 105°–115°E), with suppression of moisture transport in southern China. Dry/wet biases were thus emphasized south and north of the Yangtze River in the LowCC years. Anomalies in pentad mean geopotential height and meridional moisture flux at 850 hPa, averaged over black and blue rectangles in Fig. 7d, indicated that they rapidly increased in the third pentad of June and were higher by the end of June (Fig. S5a), which corresponds to the timing after detecting significant dry bias over southern-southeastern China in early June (Fig. 4a). In this



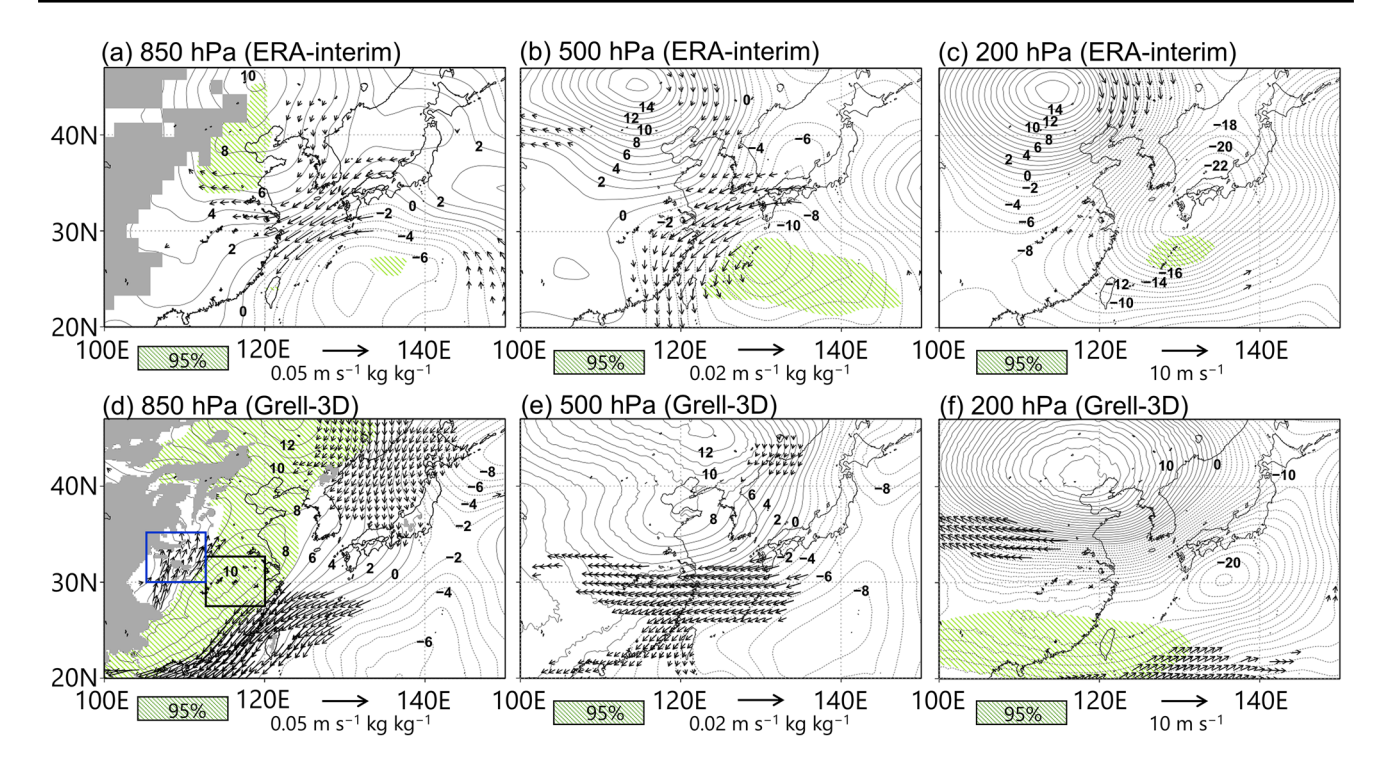
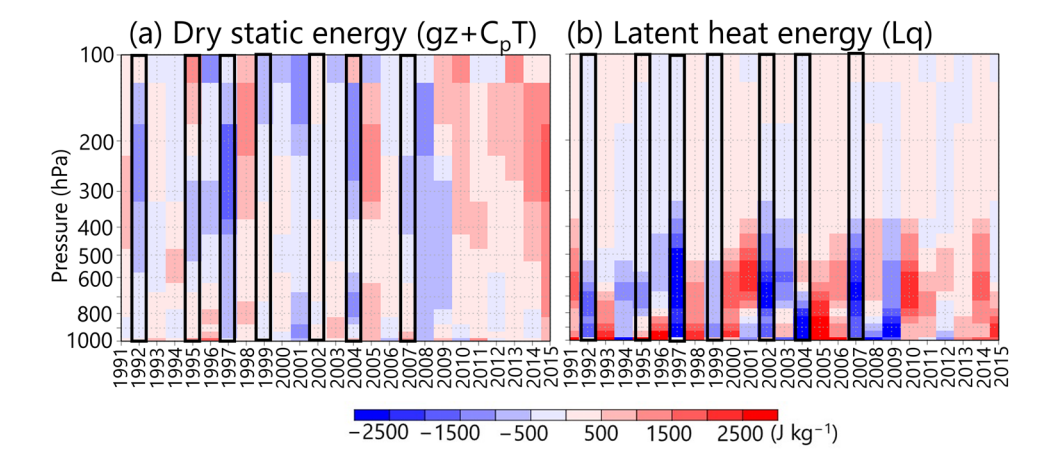


Fig. 7 Spatial distributions of anomalies in geopotential height (contours) and moisture flux or wind (vectors) in LowCC years at **a** 850 hPa, **b** 500 hPa, and **c** 200 hPa in the ERA-interim (i.e., LowCC-year composite minus the climatology for 25 years). Green hatching indicates that anomalies in geopotential height are statistically

significant at the 95% level (Student's *t*-test). Moisture flux and wind are only shown in areas with statistical significance at the 95% level. **d–f** As for (**a–c**) but for the Grell-3D experiment. Topography above 1200 m is masked in (**a–d**). Blue and black rectangles in (**d**) indicate the analysis area for Fig. S5

Fig. 8 Vertical profile of anomalies relative to the climatology of a dry static energy and b latent heat energy for each year averaged over subregion of southern-southeastern in the Grell-3D experiments. Black rectangles indicate LowCC years



period, the moisture supply to central China was enhanced in conjunction with the development of the anticyclonic circulation anomaly over southern—eastern China after the reduction of precipitation over south of the Yangtze River. This may explain the slight time gap in dry/wet bias formation between areas south and north of the Yangtze River as shown in Fig. 4a.

A comparison of synoptic-scale atmospheric circulation patterns between LowCC years and the climatology indicates that convective activity over southern-southeastern China is a key factor in enhancing dry/wet biases south and north of the Yangtze River. To further confirm the relationship between convective instability and moisture supply in LowCC years, dry static energy $(gZ+C_pT)$ and latent heat energy (Lq) were calculated for each year, where g is gravitational acceleration (9.81 m s^{-2}) , Z is geopotential height (m), C_p is heat capacity at constant pressure $(1004 \text{ J K}^{-1} \text{ kg}^{-1})$, T is temperature (K), L is latent heat $(2.5 \times 10^6 \text{ J kg}^{-1})$, and q is mixing ratio of water vapor $(kg \text{ kg}^{-1})$. Figure 8 shows vertical profiles of anomalies from the climatology, area-averaged over



southern-southeastern China. In the Grell-3D experiment, the dry static energy in LowCC years was lower than the climatology by 500-2000 J kg⁻¹ in the mid-upper troposphere (Fig. 8a), and anomalies in latent heat energy were strongly negative in the lower-mid troposphere during LowCC years (Fig. 8b). This feature was also captured in ERA-interim (except for 1999) although simulated anomalies in latent heat energy were weaker (not shown). As a result, a weakening of moist static energy $(gZ + C_pT + Lq)$ was found overall of the troposphere in LowCC years relative to that in the climatology, which was pronounced in the lower and mid-troposphere due to a reduction of latent heat energy. These results are consistent with atmospheric circulation anomalies in LowCC years being similar between reanalysis and model experiments, with moisture supply to southeastern China being further weakened in the model due to the development of anomalous anticyclonic circulation at 850 hPa in association with convection suppression. Furthermore, area-averaged June precipitation over southern-southeastern China is significantly correlated with CAPE (Fig. 9a), with LowCC years being characterized by lower precipitation and weak CAPE (red dots in Fig. 9a). This result supports the significant relationships among moisture supply, convective instability, and precipitation in June over southern-southeastern China. We suggest that the cumulus parameterization scheme influenced convective instability over southern-southeastern China during the LowCC years, as it dominated precipitation in this area (Fig. 2j). Indeed, June precipitation was not related to CAPE over central China or Japan and Korea (Fig. 9b, c), where microphysics-induced precipitation was dominant.

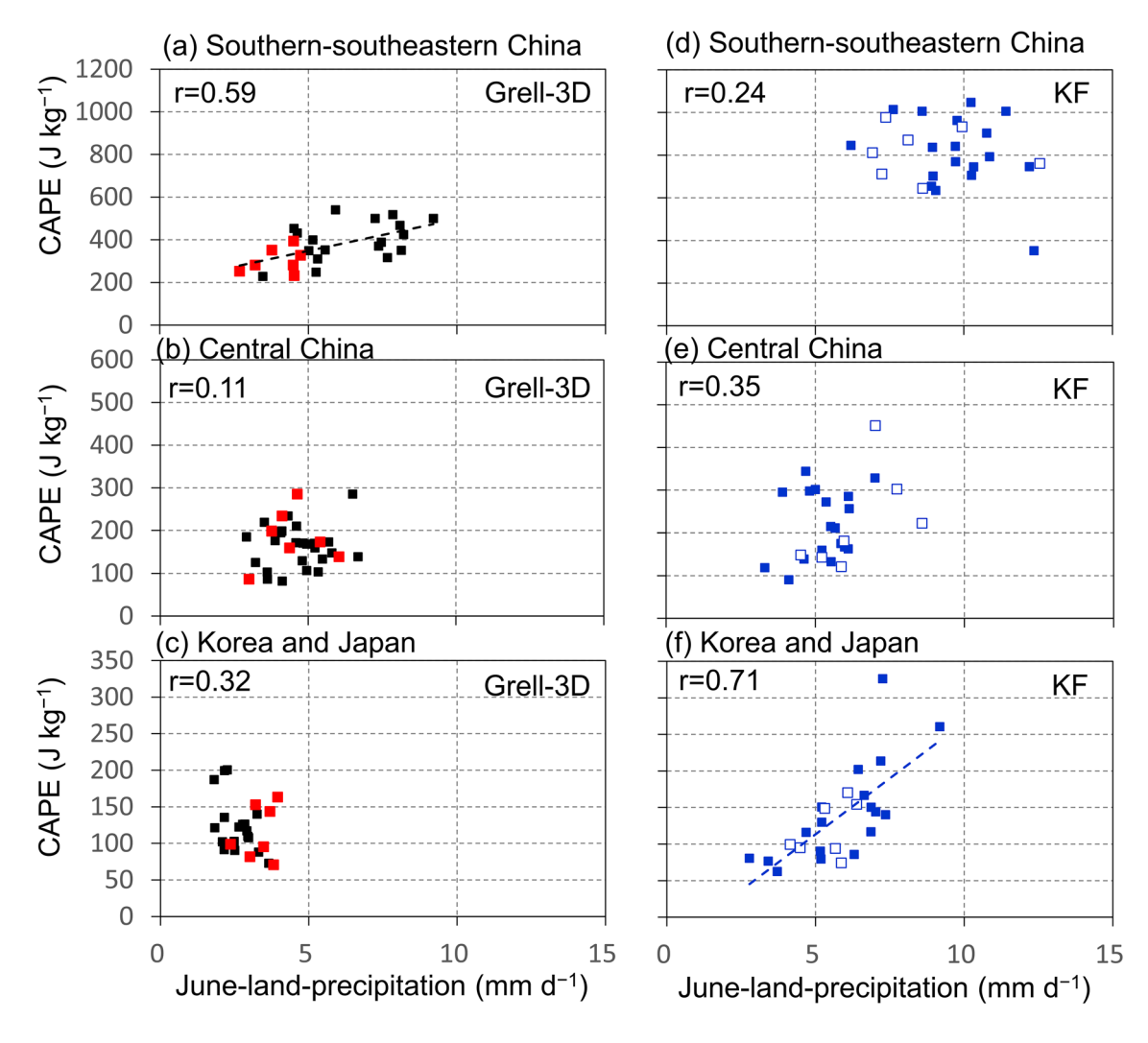


Fig. 9 Scatter-diagrams for June precipitation and CAPE averaged over land in **a** southern-southeastern China, **b** central China, and **c** Korea and Japan for the Grell-3D experiment. **d-f** As for (**a-c**) but for the KF experiment. The locations of the subregion are shown in

Fig. 1. 'r' indicates the correlation coefficient between precipitation and CAPE (the 95% significance level is 0.4). Red dots in (a-c) and white dots in (d-f) indicate the LowCC years from the original experiments



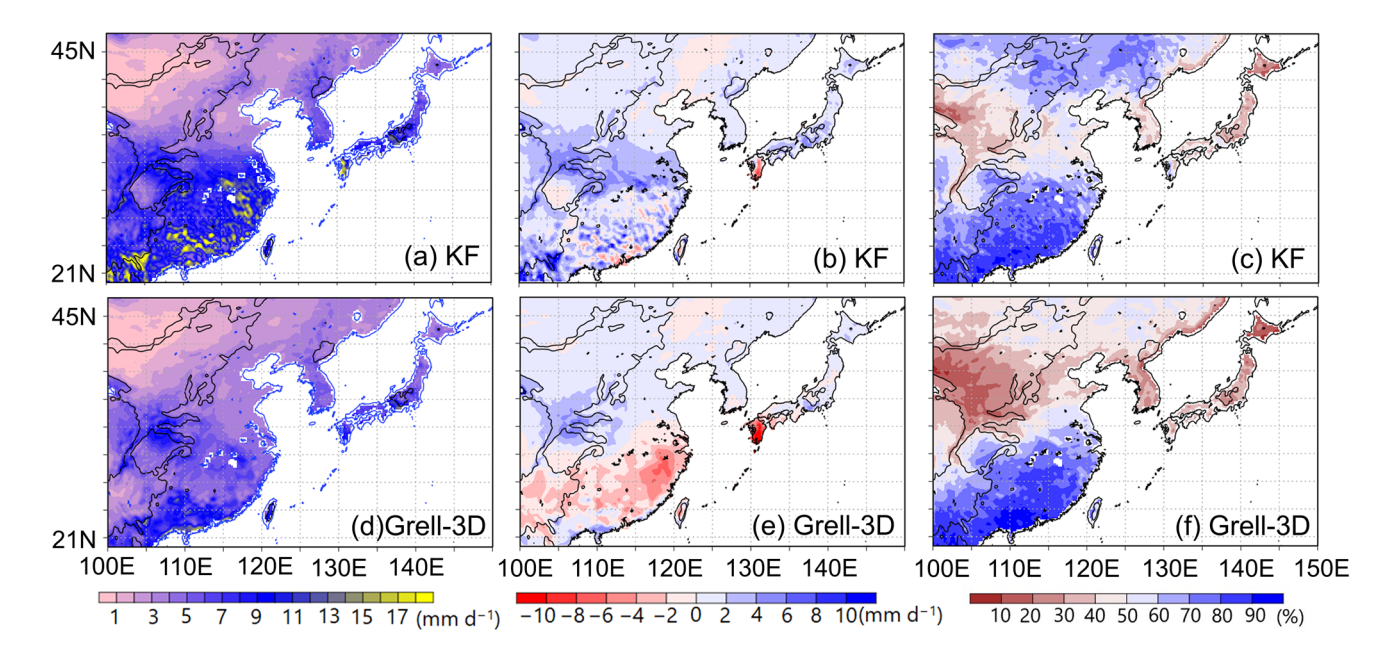


Fig. 10 a Spatial distributions of **a** monthly mean precipitation, **b** the precipitation biases (WRF—APHRODITE), and **c** the ratio of the precipitation from the cumulus parametrization to the total precipitation during June in the KF experiments. **d**–**f** As (**a**), (**b**), and

(c) but for the Grell-3D experiment, which are same as Fig. 2f, n, and j. Black contours indicate topography of 1000 and 3000 m. Ocean is masked with white color

As described in Sect. 2, in the Grell-3D ensemble scheme, several closure assumptions based on environmental stability or moisture convergence were used for dynamic control, and closure associated with moisture convergence assumes that the total precipitation rate determines the integrated vertical advection of moisture (Grell 1993). We speculate that this assumption enhances the dry bias when the anomaly of moisture transport suppression is included in the initial and lateral boundary conditions, particularly in the lower-mid troposphere. To confirm the behavior of another cumulus parameterization scheme, simulation results using the KF scheme (Kain 2004), which is one of major cumulus parameterization scheme in the WRF model and assumes closure based on CAPE removal, are discussed in Sect. 4.

4 Influences of cumulus parametrization scheme on precipitation biases in June

An experiment using the KF scheme rather than the Grell-3D ensemble scheme was undertaken to assess the effect of convective scheme on precipitation simulation. We will discuss how precipitation bias is affected with various cumulus parameterization scheme. A major difference between KF and Grell-3D is that KF does not consider the closure assumption associated with moisture convergence but assumes the closure only based on CAPE removal, i.e., environmental stability. In the KF experiment, the numerical setup was as for the Grell-3D experiment except for the

cumulus parameterization scheme (Sect. 2). Here, LowCC years are the years defined for the Grell-3D experiment (Sect. 3.1); i.e., 1992, 1995, 1997, 1999, 2002, 2004, and 2007.

Figure 10a, b shows the spatial distribution of climatological June precipitation in East Asia simulated in the KF experiment and its bias with respect to the APHRODITE dataset. Simulated June precipitation was higher in East Asia with the KF scheme than in the Grell-3D experiment, particularly over the Meiyu/Baiu front (Fig. 10a, d), which was also captured over the ocean (Fig. S6a, b). The underestimation of precipitation in the Grell-3D experiment was thus ameliorated over southern-southeastern China and southwestern Japan although its overestimation was worsened north of the Yangtze River (Fig. 10b, e and S6c, d). In the KF experiment, the pattern correlation coefficient for precipitation over land in East Asia was improved over the Grell-3D experiment not only during June but also in other months (Table 1). However, RMSE was higher in the KF experiment for all four months because the wet bias was larger in central China where climatological precipitation was low in observation (Fig. 2b). This feature of the KF experiment, with a higher pattern correlation coefficient and higher RMSE than the Grell-3D experiment, was also analyzed in June precipitation for each year (Fig. S7). The pattern correlation coefficient in LowCC years increased with the reduced underestimation of precipitation over southern-southeastern China in the KF experiment, although the dry/wet bias remained south and north of the Yangtze



River, except for 2007 (Fig. S8). A Taylor diagram shows that the simulation skill for spatial patterns of precipitation was lower in the KF experiment than that in the Grell-3D experiment (Fig. S2).

Regarding yearly variations in area-averaged precipitation during June over land in East Asia, precipitation was higher every year in the KF experiment than in APHRODITE (Fig. 3a), which is consistent with a climatological feature as discussed in the previous paragraph. The 25-yr mean and standard deviation are 5.76 and 0.55 mm d⁻¹, respectively (Table S1). The temporal correlation coefficient between APHRODITE and the KF experiment is 0.59, slightly higher than for the Grell-3D experiment (Table S2). Regarding the subregions, area-averaged precipitation over southernsoutheastern China was higher than observations except for 1995 and 2003 (Fig. 3b), with no dry bias. In central China (Fig. 3c), the wet bias is stronger in the KF experiment. The wet bias over central China tended to follow the dry bias over southern China in the Grell-3D experiment (Fig. 4a), but this relationship was not observed in the KF experiment (Figs. 4b and S5b), where an increase in precipitation over central China preceded that over southern China. Furthermore, the difference in area-averaged precipitation between the KF and Grell-3D experiments is relatively small over Japan and Korea (Fig. 3d). Temporal correlation coefficients are higher over southern-southeastern and central China in the KF experiment (0.43 and 0.35, respectively) than in the Grell-3D experiment, and worsened over Japan and Korea (0.14, respectively; Table S2).

To summarize, the dry bias over southern-southeastern China, which is obvious in the Grell-3D experiment, is reduced in the KF experiment, and the wet bias is amplified over central China. The pattern correlation coefficient is higher than for the Grell-3D experiment because of an increase in simulated precipitation over southern China. The temporal correlation coefficient for area-averaged precipitation in June over East Asia shows a slight difference between the two experiments. Although several improvements in simulated precipitation were found in the KF experiment, the simulation skill for June precipitation is higher in the Grell-3D experiment due to the excessive precipitation over central China in the former.

Two main factors controlled the simulation skill in the KF experiment: modification of the synoptic-scale circulation pattern and its influence on reduction of the dry bias over southern China; and the enhancement of the wet bias over central China. Positive biases of geopotential height at 850 hPa over central-northern China in the KF experiment is smaller than in the Grell-3D experiment, so the pressure gradient between the land of China and the western North Pacific is lower in the KF experiment (Fig. 11a). This modification in geopotential height removed

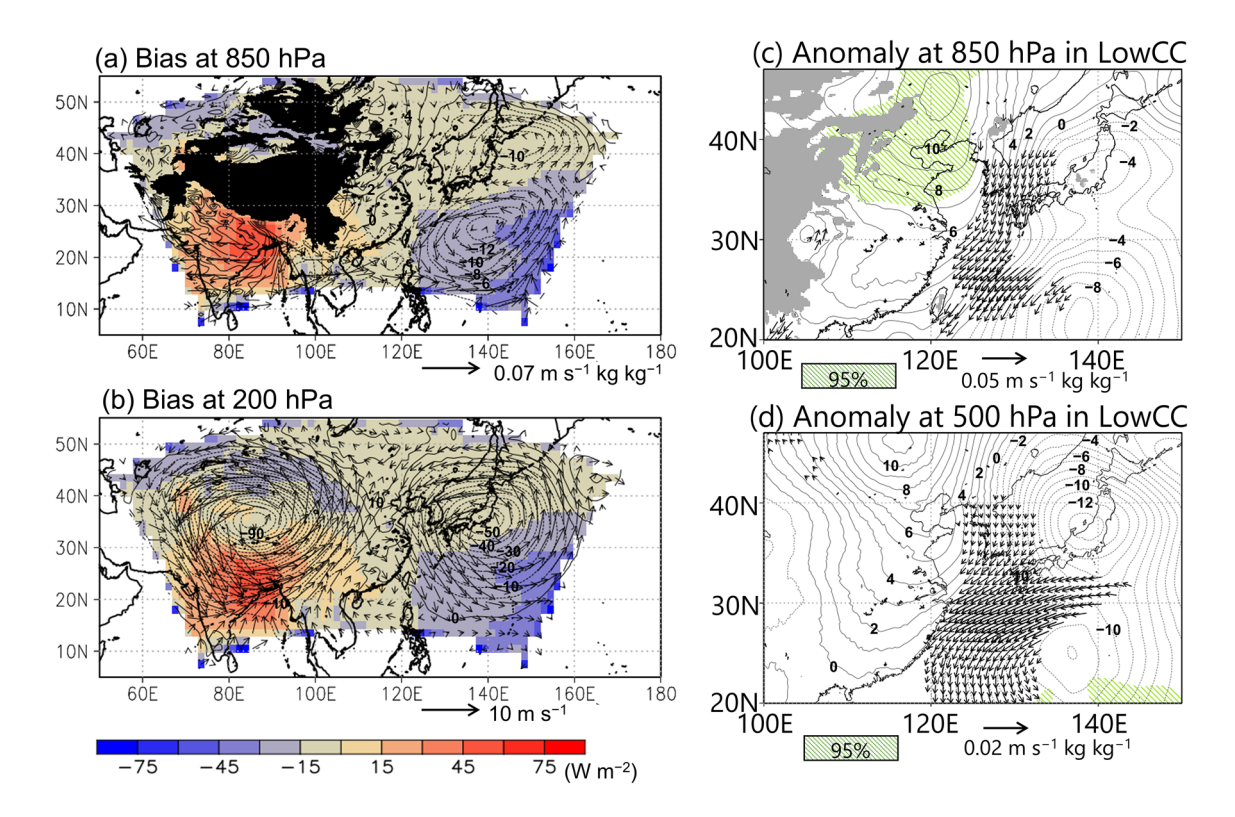


Fig. 11 As for Fig. 6b but for biases between the KF experiment and reanalysis datasets at a 850 hPa and b 200 hPa between the KF experiment and ERA-interim. c, d As for Fig. 7a but for c 850 hPa and d 500 hPa in the KF experiment. Topography above 1200 m is masked in (a) and (c)



the northeasterly biases in moisture flux not only over southern-southeastern China but also along the Meiyu/Baiu rainband, indicating that moisture transport process was improved at northern and northwestern edge of the anticyclonic circulation developed over the western North Pacific. The Taylor diagram also indicates an improvement in the spatial pattern of geopotential height at 850 hPa over southern–central China in the KF experiment (Fig. S9). At 500 hPa, the center positions of positive geopotential height bias over south of the Yangtze River and the negative bias over Japan shifted south and north, respectively, in the KF experiment relative to the Grell-3D experiment (not shown). This also resulted in weakening of the northeasterly biases in moisture flux.

The excessive convection over the western North Pacific and the inactive convection over the Indian subcontinent were identified in both the Grell-3D and KF experiments (Figs. 6b, d, 11a, b). The influence of convection biases on the large-scale circulation pattern in the troposphere, i.e., the weakening of the western North Pacific High at 850 hPa and the cyclonic circulation bias over the Tibetan Plateau at 200 hPa, were also common features in both experiments. However, the low-high-low biases in geopotential height at 850 hPa over the Pacific, which were simulated in the Grell-3D experiment, were not clear in the KF experiment (Fig. 11a). In addition, another cyclonic circulation bias also developed at 200 hPa over Japan and the western North pacific (Fig. 11b). Comparing to the Grell-3D experiment, simulated convection was more inactive in entire domain of the KF experiment except along the Meiyu/Baiu rainband and over eastern part of the Bay of Bengal (not shown). This difference in convective activity over tropical and subtropical regions may contribute to the difference in largescale circulation biases between two experiments; however, a dynamical process to explain it is beyond the scope of this study.

In addition to the modification of climatological biases in the synoptic-scale circulation pattern, the positive geopotential height anomaly at 850 hPa over southeastern China, which strongly suppressed moisture transport in this region in the Grell-3D experiment, was reduced in the KF experiment (Fig. 11c). Stagnation of moisture fluxes did not occur over southern–central China at 500 hPa because of the difference in the spatial distribution of geopotential height anomalies between the two experiments (Fig. 11d).

The climatological biases in circulation patterns and their anomalies in LowCC years suggest that the excessive weakening of moisture transport was improved in the lower-mid troposphere over southern-southeastern China in the KF experiment. As a result, CAPE was clearly higher there in the KF experiment than in the Grell-3D experiment for all 25 years (Fig. 9d). This indicates that positive feedback between inactive convection and reduced moisture inflow

was not simulated in the KF scheme, which assumes closure based on CAPE removal; consequently, the dry bias disappeared over southern China. Monthly precipitation in June was not linearly related to CAPE over southern China in the KF experiment, as was the case in the Grell-3D experiment. Since CAPE was sufficiently high (i.e., higher than 600 J kg⁻¹) in the KF experiment, the relationship between monthly-mean precipitation and CAPE may have reached climatological equilibrium.

In the Grell-3D experiment, anomalously strong northward moisture transport was simulated over northwestern area of the Sichuan Basin at 850 hPa in the LowCC years (Fig. 7d), enhancing the wet bias there. Although this moisture transport disappeared in the KF experiment (Fig. 11c), the wet bias remained and sometimes intensified over central-northern China relative to that in the Grell-3D experiment, with precipitation over the entirety of East Asia being heavier in the former than the latter (Fig. 3). This result can be attributed to the heavier precipitation derived from the KF scheme in most land areas. The ratio of precipitation from the cumulus parameterization scheme to total precipitation in the KF experiment was higher particularly over central-northern China than in the Grell-3D experiment (Fig. 10c, f), with precipitation from the microphysics scheme also increasing mainly over central-eastern China and southwestern Japan in the KF experiment (not shown). The linear correlation between June precipitation and CAPE increases over central China, as well as over Japan and Korea in the KF experiment, even though CAPE intensity is comparable to that of the Grell-3D experiment for most years (Fig. 9e, f). This result supports the inference that the precipitation amount is related to CAPE intensity over central China with the KF scheme, which assumes closure based on CAPE removal. The closure assumption of the KF scheme effectively simulates sub-gridscale precipitation overall in East Asia and also promotes further precipitation with the microphysics scheme over central China relative to the Grell-3D ensemble scheme. The wet bias is thus amplified over central China in the KF experiment even though the moisture supply from southern to central China was not simulated.

5 Summary

Experiments with a 20 km mesh were undertaken with the WRF model and Grell-3D ensemble scheme over East Asia during May–August for 1991–2015, with a focus on monthly precipitation biases. Dry biases in climatological precipitation were found along the Meiyu/Baiu rainband, while wet biases appeared south and north of the rainband. Precipitation along the rainband and to its south was controlled mainly by the cumulus parameterization scheme,

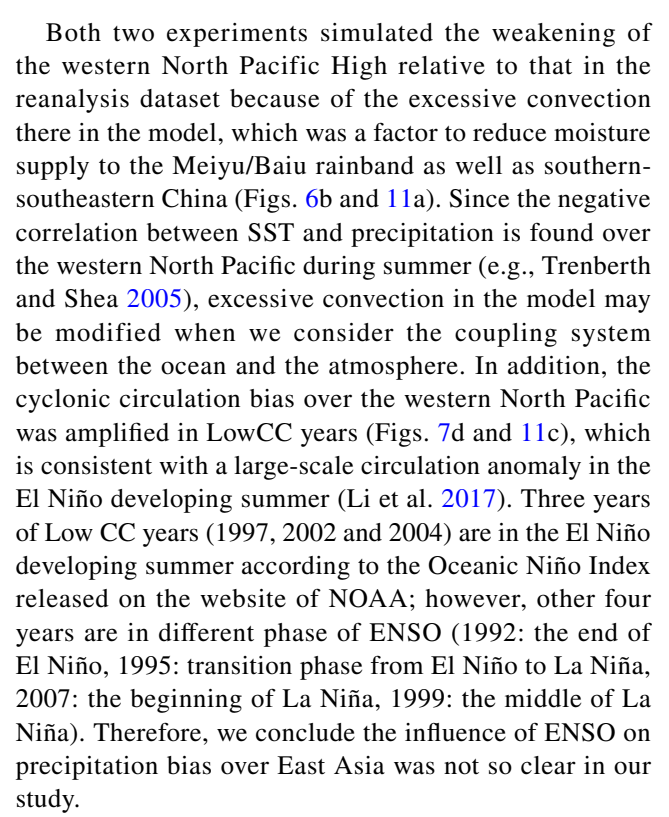


with microphysics-related precipitation being dominant north of the rainband. Precipitation biases over land during June indicate that dry and wet biases were located mainly south and north of the Yangtze River, respectively, and tended to be intensified during years of low spatial correlation with observations (LowCC years).

To elucidate how the dry/wet biases were formed in the Grell-3D experiment, climatological biases in atmospheric circulation patterns during June were compared between the reanalysis dataset and model experiments. In model experiments, the moisture supply to the Meiyu/Baiu rainband was weakened at 850 hPa due to more active convection over the western North Pacific. Anticyclonic circulation biases over northern China intensified moisture convergence there, particularly in association with biases in circulation patterns at 200 hPa expanding across the domain.

In LowCC years, moisture transport was suppressed at 850 and 500 hPa in the reanalysis dataset because of higher anomalies in geopotential height over northern China and a lower anomaly over the western North Pacific. This weakening of moisture transport was also captured in the model through the constraint of the lateral boundary conditions given by the reanalysis dataset. Anticyclonic circulation anomalies at 850 hPa over southeastern China appeared in the Grell-3D experiment along with cyclonic anomalies at 200 hPa over southern China, maintained by a positive feedback between suppressed of convection and reduced moisture supply. This anticyclonic circulation anomaly in the lower troposphere weakened moisture transport to southern-southeastern China, while intensifying moisture supply to central-northern China during LowCC years. As a result, the respective dry and wet biases south and north of the Yangtze River were emphasized in LowCC years, further intensifying biases in the climatological fields. In particular, reduced convective instability associated with weakened moisture transport was a key factor in inducing the dry bias over southern China.

Using the KF cumulus parameterization scheme, the simulated atmospheric circulation pattern was improved in the lower-mid troposphere over East Asia due to the absence of feedback between reduced moisture supply and suppressed convection over southern-southeastern China, with the dry bias particularly being reduced in this region during LowCC years. The wet bias remained and was sometimes intensified over central-northern China because the KF scheme, which assumes closure based on CAPE removal, effectively simulated precipitation related to CAPE intensity and there was an increase in precipitation from the microphysics scheme. Due to the large wet bias over central China, the simulation skill for June precipitation over land in East Asia was greater in the Grell-3D experiment than in the KF experiment.



Although we focused on precipitation biases over East Asia during June, biases in other months should also be investigated. In particular, atmospheric factors that contribute to precipitation biases in July should be analyzed because the main rainy reason in East Asia extends into July, with large biases occurring in this month (Fig. 2). As the Meiyu/Baiu rainband shifts north in July (relative to June), different circulation patterns may affect precipitation biases. The simulation domain of our experiments included the Tibetan Plateau, where differences in precipitation biases between the Grell-3D and KF experiments were small (not shown), with biases being controlled by horizontal resolution and other physical factors such as microphysics, the planetary boundary layer, and surface effects. RCM experiments have been undertaken with different numerical setups in nine participating groups of the LS4P/TPEMIP; the results have been archived at the National Tibetan Plateau/ Third Pole Environment Data Center (TPDC). Such datasets may contribute to further understanding the influence of numerical setup on simulation skill for precipitation over East Asia and the Tibetan Plateau during summer, as well as contributing to further numerical experiments with finer horizontal resolution.

Supplementary Information The online version contains supplementary material available at https://doi.org/10.1007/s00382-022-06587-5.

Acknowledgements This study was supported in part by JSPS KAKENHI Grant Number JP20K04095,



JP20H02252 and MEXT-Program for the advanced studies of climate change projection (SENTAN) Grant Number JPMXD0722680734 and contributed to the LS4P/TPEMIP project. Authors appreciate valuable comments from two anonymous reviewers. The ERA-interim data were downloaded from the website of the ECMWF (https://apps.ecmwf.int/datasets/data/interim-full-daily/levtype=sfc/). The OISST 2, the NOAA Interpolated OLR data, and the CMAP Precipitation data were provided by the NOAA/OAR/ESRL PSL, Boulder, Colorado, USA, from their Web site at (https://psl.noaa.gov/data/gridded/data.noaa.oisst.v2.highres.html; https://psl.noaa.gov/data/gridded/data.interp_OLR.html; https://psl.noaa.gov/data/gridded/data.cmap.html). The APHRODITE datasets used in this study were from the APHRODITE/APHRODITE2 project (http://aphrodite.st.hirosaki-u.ac.jp/). We referred to the Oceanic Niño Index released at (https://origin.cpc.ncep.noaa.gov/products/analysis_monitoring/ensostuff/ONI_v5.php).

Author contributions All authors contributed to the study conception and design. Material preparation, data collection, analysis, and numerical experiments were performed by SS. The first draft of the manuscript was written by SS and all authors commented on previous versions of the manuscript. All authors read and approved the final manuscript.

Funding JSPS KAKENHI Grant Number JP20K04095, JP20H02252 and MEXT-Program for the advanced studies of climate change projection (SENTAN) Grant Number JPMXD0722680734.

Availability of data and material We used the datasets described below, and this information is written in Acknowledgement. The ERA-interim: The website of the ECMWF (https://apps.ecmwf.int/datasets/data/interim-full-daily/levtype=sfc/). The OISST v2: https://psl.noaa.gov/data/gridded/data.noaa.oisst.v2.highres.html. The NOAA Interpolated OLR data: https://psl.noaa.gov/data/gridded/data.interp_OLR.html. The CMAP data: https://psl.noaa.gov/data/gridded/data.cmap.html. The APHRODITE: http://aphrodite.st.hirosaki-u.ac.jp/. The Oceanic Niño Index: https://origin.cpc.ncep.noaa.gov/products/analysis_monit oring/ensostuff/ONI_v5.php. The WRF model outputs generated and analyzed during the current study are available on request from the corresponding author.

Declarations

Conflict of interest Not applicable.

Code availability (software application or custom code) Not applicable.

Research involving humans and/or animals Not applicable.

Ethics approval Authors certify that this paper consists of original, unpublished work which is not under consideration for publication elsewhere. This is not salami-slicing work. The manuscript does not include any fabrication, falsification or inappropriate data manipulation.

Consent to participate All of authors agree to the participation in this work

Consent for publication All of authors agree to the submission and publication of this manuscript.

Open Access This article is licensed under a Creative Commons Attribution 4.0 International License, which permits use, sharing, adaptation, distribution and reproduction in any medium or format, as long as you give appropriate credit to the original author(s) and the source, provide a link to the Creative Commons licence, and indicate if changes were made. The images or other third party material in this

article are included in the article's Creative Commons licence, unless indicated otherwise in a credit line to the material. If material is not included in the article's Creative Commons licence and your intended use is not permitted by statutory regulation or exceeds the permitted use, you will need to obtain permission directly from the copyright holder. To view a copy of this licence, visit http://creativecommons.org/licenses/by/4.0/.

References

- Bao Y (2013) Simulations of summer monsoon climate over East Asia with a Regional Climate Model (RegCM) using Tiedtke convective parameterization scheme (CPS). Atmos Res 134:35–44. https://doi.org/10.1016/j.atmosres.2013.06.009
- Cai Y, Lu X, Chen G, Yang S (2018) Diurnal cycles of Mei-yu rainfall simulated over eastern China: sensitivity to cumulus convective parameterization. Atmos Res 213:236–251. https://doi.org/10. 1016/j.atmosres.2018.06.003
- Chen F, Dudhia J (2001) Coupling an advanced land surface/hydrology model with the Penn State/NCAR MM5 modeling system. Part I: model description and implementation. Mon Weather Rev 129:569–585. https://doi.org/10.1175/1520-0493(2001)129% 3c0569:CAALSH%3e2.0.CO;2
- Choi I-J, Jin EK, Han J-Y, Kim S-Y, Kwon Y (2015) Sensitivity of diurnal variation in simulated precipitation during East Asian summer monsoon to cumulus parameterization schemes. J Geophys Res Atmos 120:11971–11987. https://doi.org/10.1002/ 2015JD023810
- Dee DP et al (2011) The ERA-Interim reanalysis: configuration and performance of the data assimilation system. Q J R Meteorol Soc 137:553–597. https://doi.org/10.1002/qj.828
- Ding Q, Wang B (2005) Circumglobal teleconnection in the northern hemisphere summer. J Clim 20:3483–3505. https://doi.org/10.1175/JCLI3473.1
- Ding Q, Wang B (2007) Intraseasonal teleconnection between the summer Eurasian wave train and the Indian monsoon. J Clim 20:3751–3767. https://doi.org/10.1175/JCLI4221.1
- Dudhia J (1989) Numerical study of convection observed during the winter monsoon experiment using a mesoscale two-dimensional model. J Atmos Sci 46:3077–3107. https://doi.org/10.1175/1520-0469(1989)046%3c3077:NSOCOD%3e2.0.CO;2
- Feng X, Liu C, Rasmussen R, Fan G (2014) A 10-yr climatology of Tibetan Plateau vortices with NCEP climate forecast system reanalysis. J Appl Meteor Climatol 43:34–46. https://doi.org/10.1175/JAMC-D-13-014.1
- Fujita M, Mizuta R, Ishii M, Endo H, Sato T, Okada Y, Kawazoe S, Sugimoto S, Ishihara K, Watanabe S (2020) Precipitation changes in a climate with 2-K surface warming from large ensemble simulations using 60-km global and 20-km regional atmospheric models. Geophys Res Lett 46:435–442. https://doi.org/10.1029/2018GL079885
- Grell GA (1993) Prognostic evaluation of assumptions used by cumulus parameterizations. Mon Weather Rev 121:764–787. https://doi.org/10.1175/1520-0493(1993)121%3c0764: PEOAUB%3e2.0.CO:2
- Grell GA, Devenyi D (2002) A generalized approach to parameterizing convection combining ensemble and data assimilation techniques. Geophys Res Lett 29: Article 1693. https://doi.org/10.1029/2002GL015311
- Huang D, Gao S (2017) Impact of different cumulus convective parameterization schemes on the simulation of precipitation over China. Tellus A Dyn Meteorol Oceanogr 69:1406264. https://doi.org/10.1080/16000870.2017.1406264



- Kain JS (2004) The Kain-Fritsch convective parameterization: an update. J Appl Meteor 43:170–181. https://doi.org/10.1175/ 1520-0450(2004)043%3c0170:TKCPAU%3e2.0.CO;2
- Li Y, Yun W, Yang S, Liang H, Shouting G, Fu R (2008) Characteristics of summer convective systems initiated over the Tibetan Plateau. Part 1: origin, track, development, and precipitation. J Appl Meteorol Climatol 47:2679–2695. https:// doi.org/10.1175/2008JAMC1695.1
- Li T, Wang B, Wu B, Zhou T, Chang CP, Zhang R (2017) Theories on formation of an anomalous anticyclone in western north pacific during El Niño: a review. J Meteorol Res 31:987–1006. https://doi.org/10.1007/s13351-017-7147-6
- Liebmann B, Smith CA (1996) Description of a complete (interpolated) outgoing longwave radiation Dataset. Bull Am Meteor Soc 77:1275–1277
- Liu X, Yanai M (2002) Influence of Eurasian spring snow cover on Asian summer rainfall. Int J Climatol 22:1075–1089. https:// doi.org/10.1002/joc.784
- Mizuta R, Murata A, Ishii M, Shiogama H, Hibino K, Mori N, Arakawa O, Imada Y, Yoshida K, Aoyagi T, Kawase H, Mori M, Okada Y, Shimura T, Nagatomo T, Ikeda M, Endo H, Nosaka M, Arai M, Takahashi C, Tanaka K, Takemi T, Tachikawa Y, Temur K, Kamae Y, Watanabe M, Sasaki H, Kitoh A, Takayabu I, Nakakita E, Kimoto M (2017) Over 5000 years of ensemble future climate simulations by 60-km global and 20-km regional atmospheric models. Bull Am Meteor Soc 98(7):1383–1398. https://doi.org/10.1175/BAMS-D-16-0099.1
- Mlawer EJ, Taubman SJ, Brown PD, Iacono MJ, Clough SA (1997) Radiative transfer for inhomogeneous atmosphere: RRTM, a validated correlated-k model for the longwave. J Geophys Res-Atmos 102:16663–16682. https://doi.org/10.1029/97JD00237
- Nakanishi M, Niino H (2004) An improved Mellor-Yamada level-3 model: its design and verification. Boundary Layer Meteor 112:1–31. https://doi.org/10.1023/B:BOUN.0000020164.04146.
- Nakanishi M, Niino H (2006) An improved Mellor-Yamada level-3 model: its numerical stability and application to a regional prediction of advecting fog. Boundary Layer Meteorol 119:397– 407. https://doi.org/10.1007/s10546-005-9030-8
- Nguyen-Le D, Yamada TJ, Tran-Anh D (2017) Classification and forecast of heavy rainfall in northern Kyushu during Baiu season using weather pattern recognition. Atmos Sci Lett 18:324–329. https://doi.org/10.1002/asl.759
- Niu X, Tang J, Wang S, Fu C, Chen D (2020) On the sensitivity of seasonal and diurnal precipitation to cumulus parameterization over CORDEX-EA-II. Clim Dyn 54:373–393. https://doi.org/10.1007/s00382-019-05010-w
- Nitta T (1987) Convective activities in the tropical western Pacific and their impact on the northern hemisphere summer circulation. J Meteor Soc Japan 65:373–390. https://doi.org/10.2151/jmsj1965.653.373
- Ohba M, Kadokura S, Yoshida Y, Nohara D, Toyoda Y (2015) Anomalous weather patterns in relation to heavy precipitation events in Japan during the Baiu season. J Hydrometeor 16:688– 701. https://doi.org/10.1175/JHM-D-14-0124.1
- Reynolds RW, Smith TM, Liu C, Chelton DB, Casey KS, Schlax MG (2007) Daily high resolution blended analysis for sea surface temperatures. J Clim 20:5473–5496. https://doi.org/10.1175/2007JCLI1824.1
- Sato T, Xue Y (2013) Validating a regional climate model's downscaling ability for East Asian summer monsoonal interannual variability. Clim Dyn 41:2411–2426. https://doi.org/10.1007/s00382-012-1616-5
- Seol K-H, Hong S-Y (2009) Relationship between the Tibetan snow in spring and the East Asian summer monsoon in 2003: a global

- and regional modeling study. J Clim 22:2095–2110. https://doi.org/10.1175/2008JCLI2496.1
- Shing GP, Oh J-H, Kim J-Y, Kim O-Y (2006) Sensitivity of summer monsoon precipitation over East Asia to convective parameterization schemes in RegCM3. SOLA 2:029–032. https:// doi.org/10.2151/sola.2006-008
- Skamarock WC, Klemp JB, Dudhia J, Gill DO, Barker DM, Duda MG, Huang XY, Wang W, Powers JG (2008) A description of the advanced research WRF version 3. NCAR Technical Note. NCAR/TN-475+STR
- Sugimoto S (2020) Heavy precipitation over southwestern Japan during the Baiu season due to abundant moisture transport from synoptic-scale atmospheric conditions. SOLA 16:17–22. https://doi.org/10.2151/sola.2020-004
- Sui C-H, Chung P-H, Li T (2007) Interannual and interdecadal variability of the summertime western North Pacific subtropical high. J Geophys Res Atmos 34:L11701. https://doi.org/10.1029/ 2006GL029204
- Takahashi HG, Fujinami H (2021) Recent decadal enhancement of Meiyu-Baiu heavy rainfall over East Asia. Sci Rep 11:13665. https://doi.org/10.1038/s41598-021-93006-0
- Thompson G, Field PR, Rasmussen RM, Hall WD (2008) Explicit forecasts of winter precipitation using an improved bulk microphysics scheme. Part II: implementation of a new snow parameterization. Mon Weather Rev 136:5095–5115. https://doi.org/10.1175/2008MWR2387.1
- Trenberth KE, Shea DJ (2005) Relationships between precipitation and surface temperature. Geophys Res Lett 32:L14703. https://doi.org/10.1029/2005GL022760
- Wu T-W, Qian Z-A (2003) The Relation between the Tibetan winter snow and the Asian summer monsoon and rainfall: an observational investigation. J Clim 16:2038–2051. https://doi.org/10.1175/1520-0442(2003)016%3c2038:TRBTTW%3e2.0.CO;2
- Xiao Z, Duan A (2016) Impacts of Tibetan Plateau snow cover on the interannual variability of the East Asian summer monsoon. J Clim 29:8495–8514. https://doi.org/10.1175/JCLI-D-16-0029.1
- Xie P, Arkin PA (1997) Global precipitation: a 17-year monthly analysis based on gauge observations, satellite estimates, and numerical model outputs. Bull Am Meteor Soc 78:2539–2558. https://doi.org/10.1175/1520-0477(1997)078%3c2539: GPAYMA%3e2.0.CO;2
- Xue Y, Diallo I, Li W, Neelin JD, Chu PC, Vasic R, Guo W, Li Q, Robinson DA, Zhu Y, Fu C, Oaida CM (2018) Spring land surface and subsurface temperature anomalies and subsequent downstream late spring-summer droughts/floods in North America and East Asia. J Geophys Res Atmos 123:5001–5019. https://doi.org/10.1029/2017JD028246
- Xue Y et al (2021) Impact of initialized land surface temperature and snowpack on subseasonal to seasonal prediction project, Phase I (LS4P-I): organization and experimental design. Geosci Model Dev 14:4465–4494. https://doi.org/10.5194/gmd-14-4465-2021
- Yasunari T, Miwa T (2006) Convective cloud systems over the Tibetan Plateau and their impact on meso-scale disturbances in the Meiyu/Baiu frontal zone—a case study in 1998. J Meteor Soc Japan 84:783–803. https://doi.org/10.2151/jmsj.84.783
- Yatagai A, Arakawa O, Kamiguchi K, Kawamoto H, Nodzu MI, Hamada A (2009) A 44-year daily gridded precipitation dataset for Asia based on a dense network of rain gauges. SOLA 5:137– 140. https://doi.org/10.2151/sola.2009-035
- Yatagai A, Kamiguchi K, Arakawa O, Hamada A, Yasutomi N, Kitoh A (2012) APHRODITE: constructing a long-term daily gridded precipitation dataset for Asia based on a dense network of rain gauges. Bull Am Meteor Soc 93:1401–1415. https://doi.org/10.1175/BAMS-D-11-00122.1



- Yihui D, Chan CL (2005) The East Asian summer monsoon: an overview. Meteorol Atmos Phys 89:117–142. https://doi.org/10.1007/s00703-005-0125-z
- Yu K, Hui P, Zhou W, Tang J (2020) Evaluation of multi-RCM highresolution hindcast over the CORDEX East Asia Phase II region: mean, annual cycle and interannual variations. Int J Climatol 40:2134–2152. https://doi.org/10.1002/joc.6323
- Zhang S, Lu S, Bao Y, Ma D (2015) Sensitivity of precipitation over China to different cumulus parameterization schemes in RegCM4. J Meteorol Res 29:119–131. https://doi.org/10.1007/s13351-014-4042-2
- Zhao P, Zhou Z, Liu J (2007) Variability of Tibetan spring snow and its associations with the hemispheric extratropical circulation and East Asian summer monsoon rainfall: an observational investigation. J Clim 20:3942–3955. https://doi.org/10.1175/JCL14205.1

Publisher's Note Springer Nature remains neutral with regard to jurisdictional claims in published maps and institutional affiliations.

